

Comprehensive Status Report: November 18, 2004

Project Title: Deepwater Riser VIV Project – CFD Simulation of Riser VIV
MMS Project: 481 TO Number: 74521
PI: Hamn-Ching Chen, Chia-Rong Chen, Richard Mercier
COTR: A. Konczvald

This report provides a comprehensive summary of the research completed in the prior Phase of this project (September 2003 – August 2004), and describes research being done in the present Phase (September 2004 – August 2005).

CFD Simulation of Riser VIV

**Hamn-Ching Chen, Chia-Rong Chen, Richard S. Mercier, Juan P. Pontaza
(Researcher)**

1. Project Description

1.1 Background

Offshore oil/gas drilling and production face hazards due to the exposure of submerged rig components to underwater sea currents. Critical among these components are the marine risers, consisting of a series of long steel pipes of circular cross-section, used for deep-water extraction of oil and/or natural gas. These long cylindrical structures, exposed to strong sea currents, induce the flow around them to separate and initiate vortex shedding – whereby vortices of opposite sign are shed synchronously from the aft of the structure. The resultant lift and drag forces excite forced oscillations of the cylinder, known as vortex-induced vibrations (VIV). When the VIV frequency is close to one of the natural frequencies of the structure, a resonance phenomenon popularly known as “lock-in” occurs, resulting in enhancement of the vibration amplitude of the structure – and thus its destructive potential.

Currently, the design criteria and tools for the operation of marine risers under lock-in conditions rely in simplified mathematical models and/or anecdotal evidence. Increasing development costs and increasingly hostile field environments, demand more robust, reliable, and refined design strategies and tools. This need has renewed interest in the study of the VIV phenomenon, by experimentalists and numerical analysts.

In operating conditions, the marine risers are subjected to flow conditions that correspond to high Reynolds number flows, typically $O(10^5)$ – $O(10^7)$ and low structural damping. These conditions are hard and expensive to achieve in an experimental setup, and thus an attractive alternative is to use computational fluid dynamics (CFD) tools to verify/predict the response of the cylinder undergoing VIV. Unfortunately, well-established numerical procedures for CFD (e.g., finite elements, finite differences, and control volumes) are not robust with respect to high Reynolds number flows. As the Reynolds number increases, these methods are prone to developing spurious node-to-node oscillations – which eventually cause the numerical solution procedure to break down. The oscillations can be suppressed by refining the mesh, but the necessary degree of refinement is often prohibitively expensive. In view of this drawback, most of

the previous work on simulations of the VIV phenomena have been limited to low Reynolds number flow, $O(10^2) - O(10^3)$, and allowing only for single degree of freedom motions.

1.2 Present Work

The main thrust of this work is to use a novel discretization procedure, whereby the Navier-Stokes equations are discretized using local analytic solutions of the linearized problem. The formulation is robust with respect to high Reynolds number flows, strong mesh skews, and is asymptotically second-order accurate. In addition, the formulation is implemented alongside the ability to treat embedded and non-matching grids, allowing for relative grid motion. This capability makes fluid-structure interaction problems easy to handle, as tedious grid re-generation is avoided by virtue of the ability to treat embedded meshes moving in fixed background grid components. Thus, the formulation is suitable to simulate the VIV phenomena – inherently a fluid-structure interaction problem at high Reynolds numbers.

The objective of this research is to focus on the development of advanced CFD capabilities (such as the one described above) for improving the prediction of riser VIV responses at high Reynolds number and under three-dimensional sheared currents. In this project, the method will be further extended to assess the effects of Reynolds numbers, surface roughness, ambient turbulence, and highly sheared currents on riser VIV responses. The performance of VIV suppression devices such as helical strakes and fairings will also be evaluated. The simulation results will be compared with available experimental data to assess the performance of various roughness and turbulence models for VIV predictions.

2. Progress and Results

The progress to date is presented as descriptions of the following tasks:

- Development of advanced CFD capabilities
- Simulations for flow past a fixed circular cylinder at high Reynolds number
- Surface roughness effects
- Simulations of circular cylinders undergoing VIV at high Reynolds number
- Large eddy simulation of three-dimensional flow past a fixed circular cylinder

2.1 Development of Advanced CFD Capabilities

The discretization procedure for the numerical solution of the incompressible Navier-Stokes equations was revised and further enhanced with a revised pressure solver and robust linear algebraic solvers. The procedure was tested through a series of well-established verification and validation benchmarks to ensure and demonstrate its robustness with respect to (1) high Reynolds number flows, (2) strong mesh skews, and (3) high aspect ratio cells. This task by itself, we believe, is of great value – as it gives us increased confidence in the capabilities of the formulation. A description of the formulation and detailed numerical results for the set of two- and three-dimensional verification and validation benchmarks was documented and reported in [1].

2.2 Simulations for Flow Past a Fixed Circular Cylinder

We consider the two-dimensional flow of an incompressible fluid past a smooth circular cylinder. At low Reynolds numbers ($5 < \text{Re} < 40$) the flow is stationary and characterized by a pair of standing vortices appearing behind the cylinder. The size of the separated flow region increases with increasing Reynolds number, until a limit in which the wake becomes unstable. At this critical Reynolds number, $\text{Re}_c \approx 46.2$, vortices are shed from the aft of the circular cylinder, forming the well-known von Karman vortex street.

We wish to test the predictive capabilities of the formulation for a wide range of Reynolds numbers, and especially at high Reynolds numbers. To this end we perform a set of simulations spanning the Reynolds number range $O(10^1) - O(10^7)$ which covers sub-, trans-, super-, and post-critical flow regimes for separated flows around bluff bodies. In spite of the fact that the flow is no longer two-dimensional above $\text{Re}_c^{3-D} \approx 188.5$, we expect the simulation results to qualitatively follow experimentally observed behavior.

The computational domain is an overset (Chimera) grid, consisting of four overlapping and embedded grid systems. The first grid, $\bar{\Omega}_1^h = [-15.5, 20.5] \times [-15.5, 15.5]$, is a background mesh with uniform spacing $\Delta x = \Delta y = 0.25$. The second grid, $\bar{\Omega}_2^h = [-3.0, 10.0] \times [-3.0, 3.0]$, is embedded in $\bar{\Omega}_1^h$ and is a mesh with uniform spacing $\Delta x = \Delta y = 0.10$ for the purpose of resolving the far-wake flow field. The third grid, $\bar{\Omega}_3^h = [-2.0, 3.0] \times [-2.0, 2.0]$, is embedded in $\bar{\Omega}_2^h$ and is a mesh with uniform spacing $\Delta x = \Delta y = 0.05$ for the purpose of resolving the near-wake flow field immediately behind the circular cylinder. The fourth grid, $\bar{\Omega}_4^h$, is a cylindrical mesh centered at $(0,0)$ with inner radius 0.5 and outer radius 1.0, and is embedded in the Cartesian grids. This grid component is refined in the circumferential and radial directions as the Reynolds number is increased, up to a maximum size of 181×51 . The nodes in the circumferential direction are equi-spaced and the node distribution in the radial direction is such that a near wall spacing of $1/\text{Re}$ is maintained, to adequately resolve viscous near-wall effects. Thus, we consider cell aspect ratios in the near wall region of the order $1:10^5$. We find that the formulation is insensitive to such high cell aspect ratios, further attesting to its robustness. The overset grid is shown in Figure 1.

The temporal terms are discretized by the generalized α -method (GAM) family of approximations, which retain second-order accuracy in time. Simulations were performed using time step sizes of $\Delta t = 0.050, 0.020, 0.010$ and 0.005 at the highest Reynolds numbers – to ensure time step size independent solutions.

Figure 2 shows the computed *Drag* vs. *Reynolds number* data, alongside data from experimental measurements. Also plotted are two-dimensional numerical simulation results using a high-order finite element formulation, stable up to a low maximum Reynolds number of 1,000.

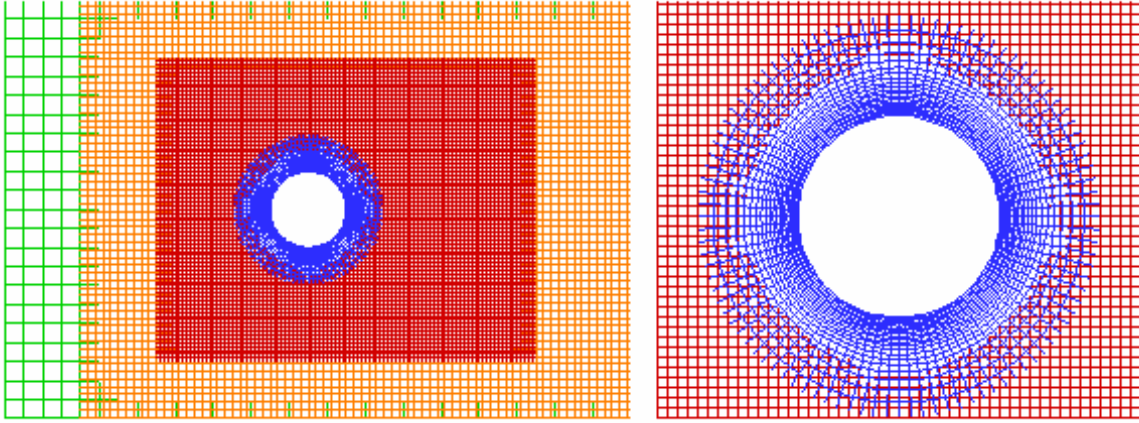


Figure 1: Partial view of the overset grid for flow past a circular cylinder. The overset grid consists of four overlapping and embedded grid systems.

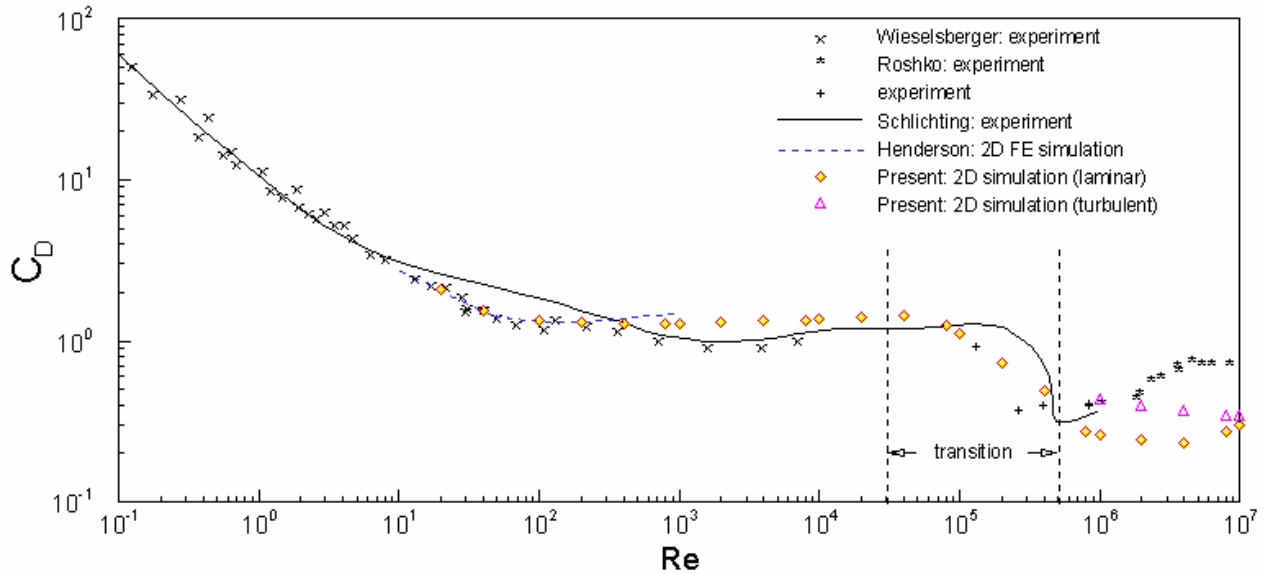


Figure 2: Drag coefficient for a smooth cylinder as a function of Reynolds number.

We see very good qualitative agreement with the experimental measurements throughout the entire Reynolds number range considered, and are able to predict the drag crisis that occurs during critical transition and the super-critical flow regime, in addition to the drag recovery in the post-critical regime. No turbulence model was used for the simulations labeled as “laminar”, so in essence they were ran as direct-numerical simulations, although we do not claim them as such – because the grid was not fine enough to resolve all scales.

Figures 3 and 4 show instantaneous vorticity contours and time histories of the drag coefficient for flow conditions in the (a) sub-critical regime, (b) critical-transition regime, (c) super-critical regime, and (d) post-critical regime. Clearly, the vortex street and drag history in each of the regimes is distinct from each other. Also shown in Figure 3, are the overset grid boundaries, signaling transition between grid components with different spatial resolution. Even

though the vorticity field is post-computed from the velocity field, independently in each grid component, we see smooth transitions between grid components. Some noise is evident at $x = 10.0$, where transition to the coarsest grid component occurs, and is due to the abrupt change in length scales used to post-compute the vorticity.

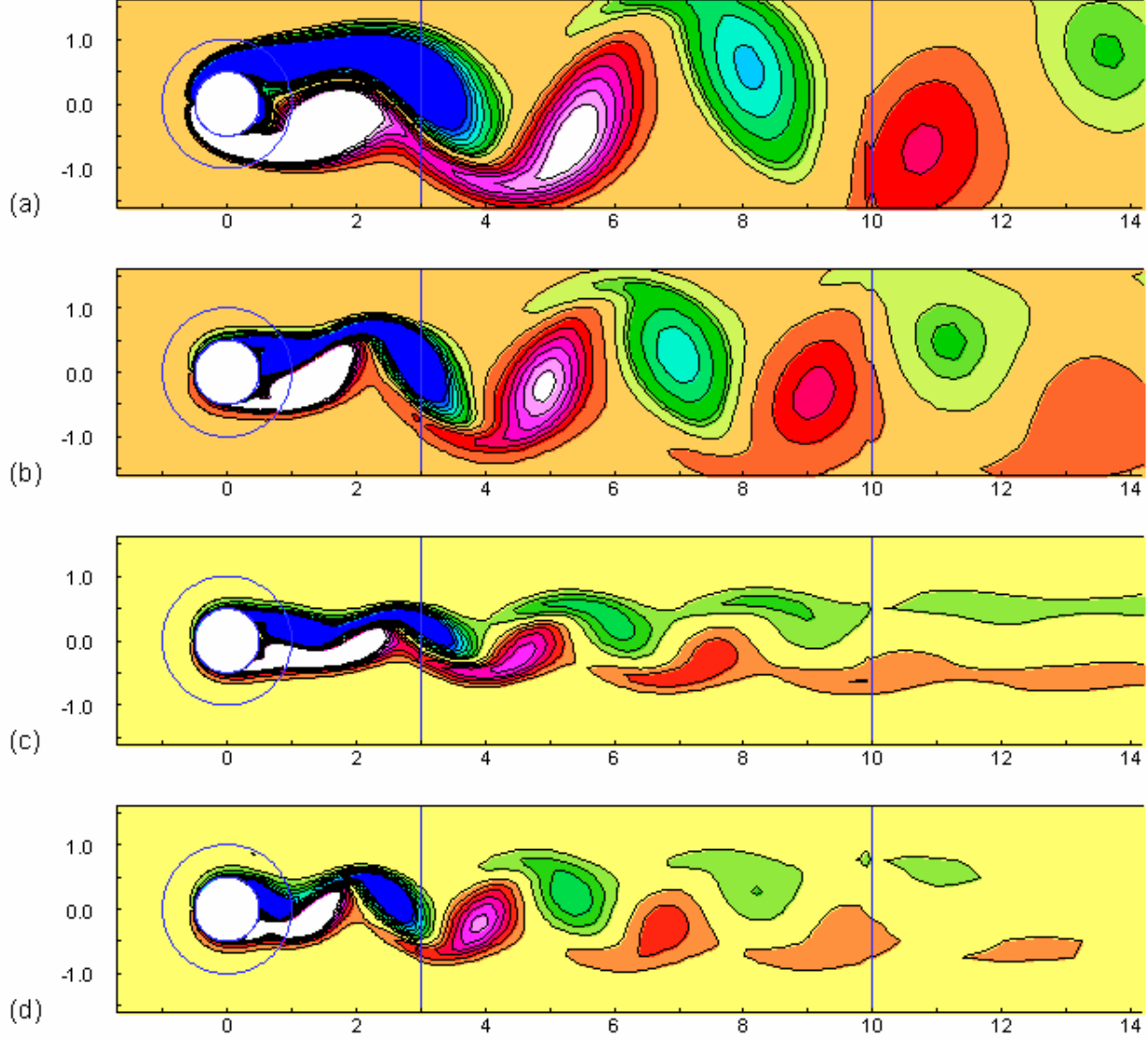


Figure 3: Instantaneous vorticity contours in the periodic steady-state for: (a) $Re = 100$, (b) $Re = 1 \times 10^5$, (c) $Re = 1 \times 10^6$, (d) $Re = 1 \times 10^7$. Also shown are the overset grid boundaries, signaling transition between different grid components.

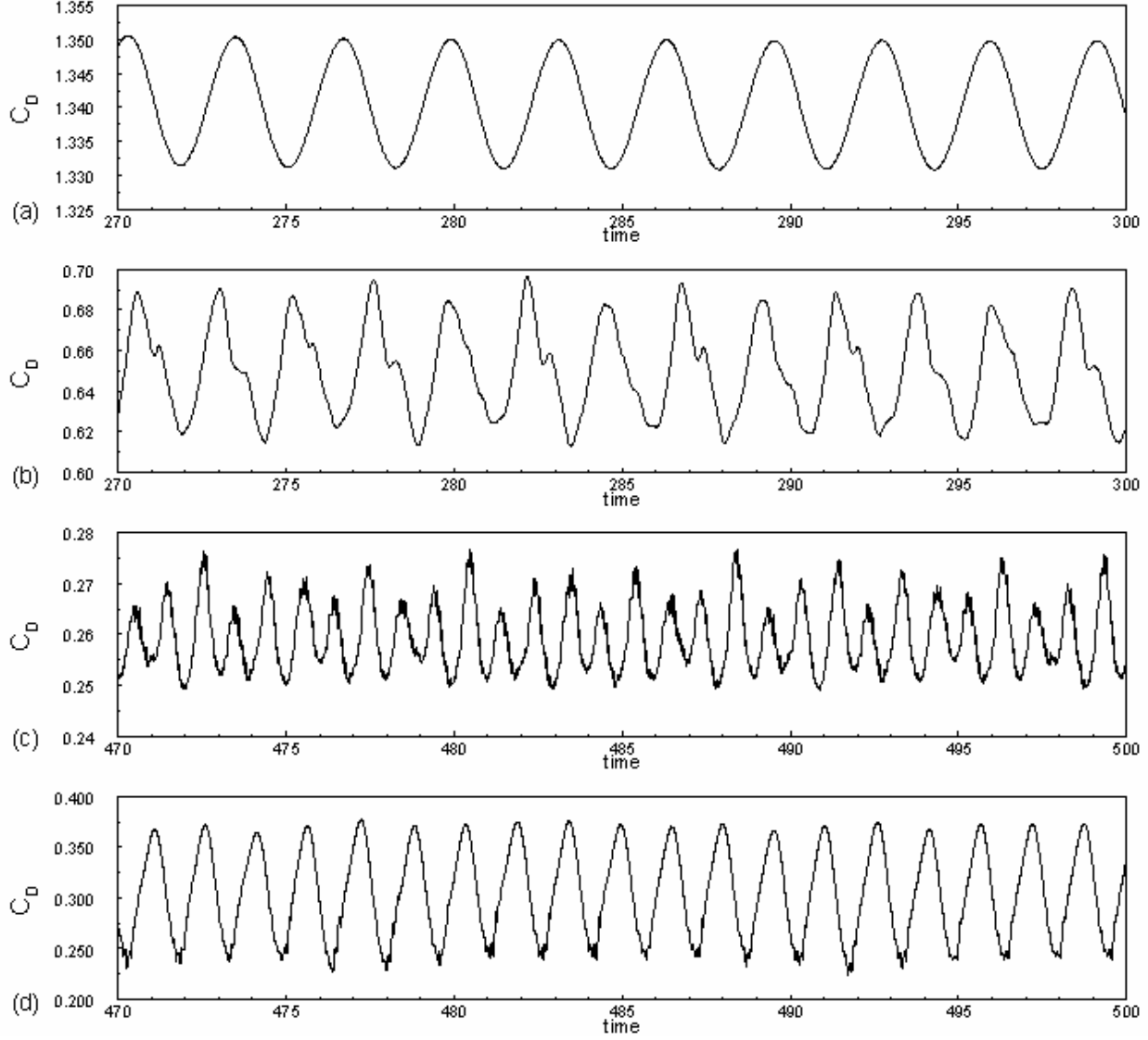


Figure 4: Time history of drag coefficient in the periodic steady-state for (a) $Re = 100$, (b) $Re = 1 \times 10^5$, (c) $Re = 1 \times 10^6$, (d) $Re = 1 \times 10^7$.

2.3 Surface Roughness Effects

A considerable amount of time was allocated to review and implement roughness models available in the open literature. Here, we document results using a two-layer $k - \varepsilon$ turbulence model with surface roughness modifications and a two-layer $k - \omega$ model with surface roughness boundary conditions.

The two-layer $k - \varepsilon$ turbulence model makes use of the standard $k - \varepsilon$ turbulence model away from the solid surface and switches to a one-equation $k - \ell$ model in the near-wall region, where the length scale is determined analytically through van-Driest type damping functions that enforce the asymptotically correct behavior as the wall is approached. The van-Driest type functions are parametrized in terms of a velocity scale based on the turbulent kinetic energy, which is well

defined during separation, rendering the model suitable for simulations where significant separation occurs. Unfortunately, the surface roughness modifications for the two-layer $k - \varepsilon$ turbulence model are parametrized in terms of the wall-shear stress, which is ill-defined during separation.

The two-layer $k - \omega$ turbulence model makes use of the standard $k - \varepsilon$ turbulence model away from the solid surface and switches to a $k - \omega$ model in the near-wall region. Thus, in the near-wall region a two-equation approach is retained. Modifications to model surface roughness are not needed, since the effects are readily accounted for by simply making use of “rough-wall” boundary conditions for ω . Unfortunately, the surface roughness boundary condition is directly correlated with the wall-shear stress, which is ill-defined for separated flows.

The flow past a circular cylinder is a flow with massive separation, and thus it was found after extensive experimentation, that roughness models parametrized in terms of the wall-shear stress are not suitable for our simulations. Figure 5 shows the time history of the drag coefficient at $Re = 1 \times 10^6$, for a smooth and rough cylinder, computed using the two-layer $k - \varepsilon$ model. In accordance with experimental data, at this Reynolds number, the effect of surface roughness is to increase the drag coefficient. However, the observed increase in drag is less pronounced than that observed in experiments for the same flow conditions and roughness ($k_s/D = 0.0025$).

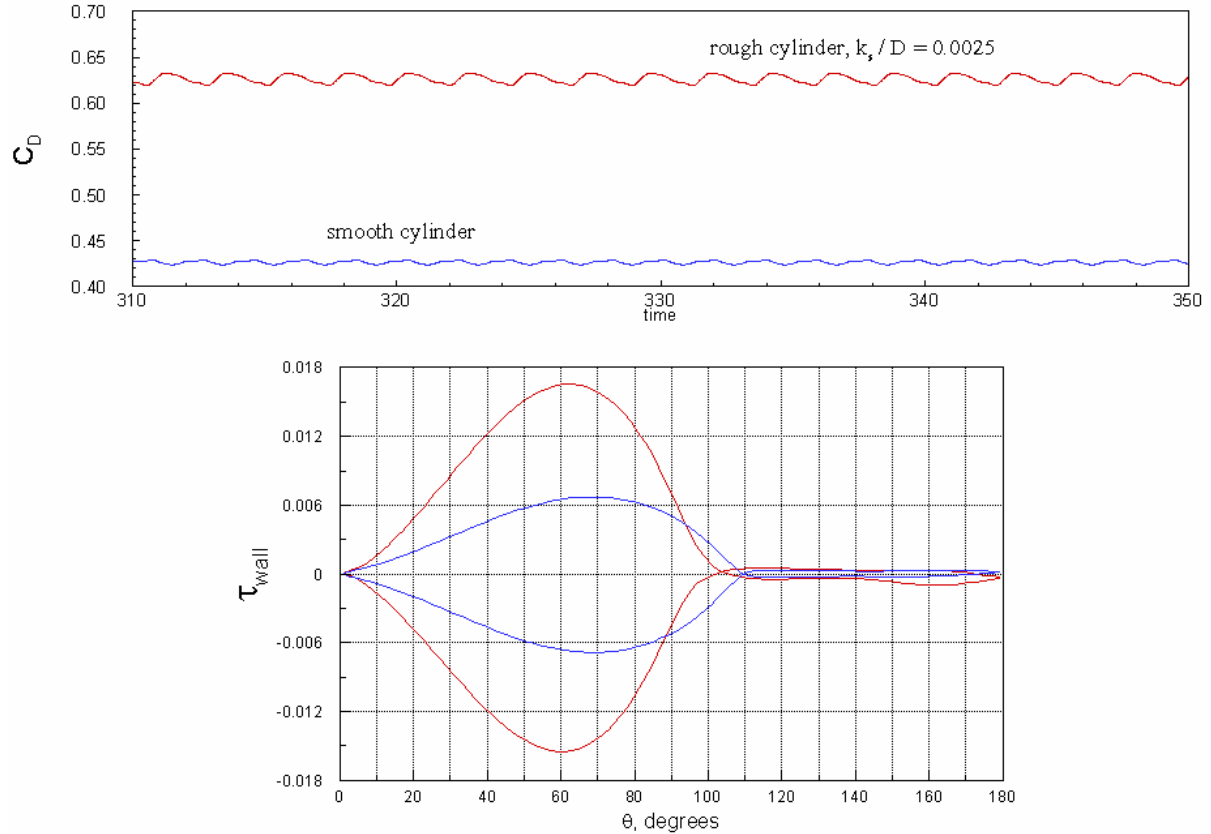


Figure 5: Surface roughness effects for flow past a circular cylinder at $Re = 1 \times 10^6$.

Thus, our plans are to propose a *new* roughness model parametrized in terms of the turbulent kinetic energy, which remains well-defined even for massively separated flows. We expect to obtain much better predictions with such a roughness model.

2.4 Simulations of Circular Cylinders Undergoing VIV

We model the VIV problem as a fluid-structure interaction problem, where the cylinder moves as a rigid body in the flow field. Given the instantaneous drag and lift acting on the cylinder surface (from the fluid-flow solution), the equations of motion governing the x - and y -displacements are integrated in time using a fourth-order Runge-Kutta scheme to determine the instantaneous response of the cylinder. In dimensionless form, the equations of motion are

$$\begin{aligned}\ddot{x} + \frac{4\pi\zeta^*}{U^*} \dot{x} + \left(\frac{2\pi}{U^*}\right)^2 x &= \frac{2}{\pi} \frac{C_D(t)}{m^*}, \quad \dot{x}(0) = x(0) = 0 \\ \ddot{y} + \frac{4\pi\zeta^*}{U^*} \dot{y} + \left(\frac{2\pi}{U^*}\right)^2 y &= \frac{2}{\pi} \frac{C_L(t)}{m^*}, \quad \dot{y}(0) = y(0) = 0\end{aligned}$$

where the dimensionless parameters m^* , ζ^* and U^* are the structural mass ratio, damping ratio, and reduced velocity, respectively.

Here we consider two-dimensional simulations using typical (realistic) flow conditions experienced by a riser, corresponding to $\text{Re} = 1 \times 10^5$ and $\text{Re} = 1 \times 10^6$, $m^* = 1.0$, $m^* \zeta^* = 0.005$, $U^* = 6.055$, and allowing for 2-dof motions. The $\text{Re} = 1 \times 10^5$ simulation is performed using no turbulence model, as the boundary layer at this Reynolds number is undergoing transition from laminar to turbulent. At $\text{Re} = 1 \times 10^6$ the boundary layer is safely assumed to be fully turbulent, and we use a two-layer $k - \varepsilon$ model to account for the effects of turbulence.

The cylinder is first held stationary until a periodic steady-state is well established – at which point the cylinder is “released” and allowed to respond to the flow field. Figure 6 shows the time history of the x and y displacements of the cylinder at flow conditions of $\text{Re} = 1 \times 10^5$. Evidently, strong vortex-induced vibrations occur, with cross-stream amplitudes as high as 2.0 cylinder diameters. It is further noted that the cross-stream oscillations are much more regular than the in-line oscillations. During time intervals when the in-line oscillations become regular about a mean value, the motions of the cylinder settle down into the well-known “figure-eight” shape (Fig. 6). The resulting “figure-eight” has maximum cross-stream amplitudes of 1.65 cylinder diameters and maximum in-line amplitudes of 0.70 cylinder diameters.

Figure 7 shows the time history of the x and y displacements of the cylinder at flow conditions of $\text{Re} = 1 \times 10^6$. The response is more regular than in the previous case at $\text{Re} = 1 \times 10^5$, due to the time-averaging of fluctuations inherent in the Reynolds-averaged Navier-Stokes equations. The motions of the cylinder settle down into a tight “figure-eight” shape, as shown.

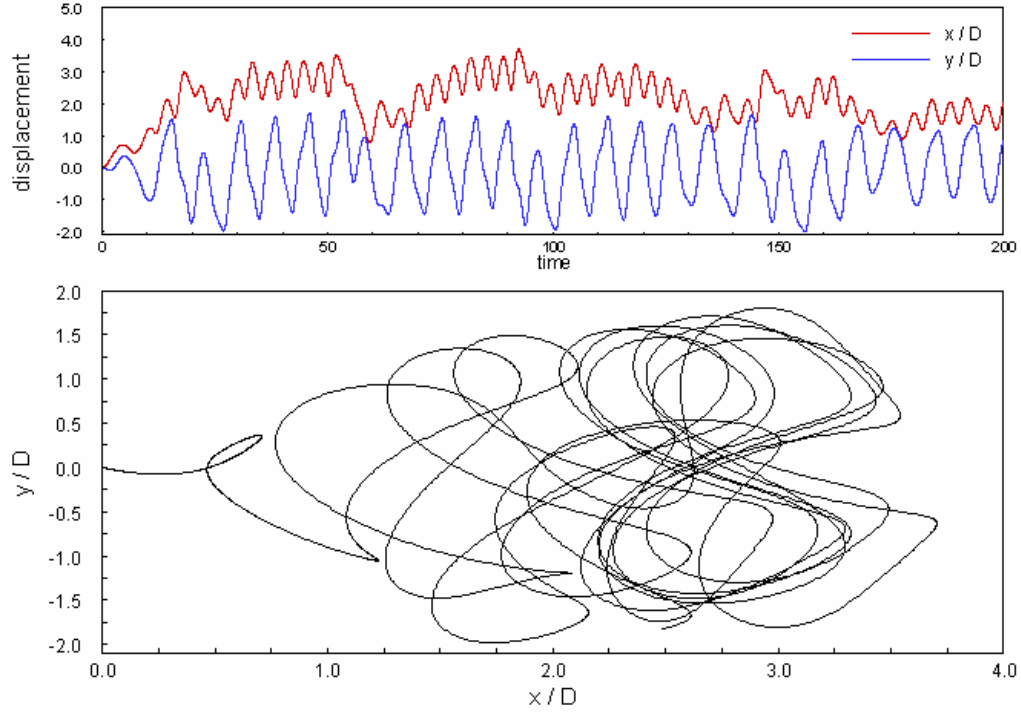


Figure 6: Circular cylinder undergoing VIV at $Re = 1 \times 10^5$. (a) Time history of cylinder's cross-stream and in-line displacements. (b) Trajectory of the cylinder in $x - y$ space for $t \in [0, 500]$.

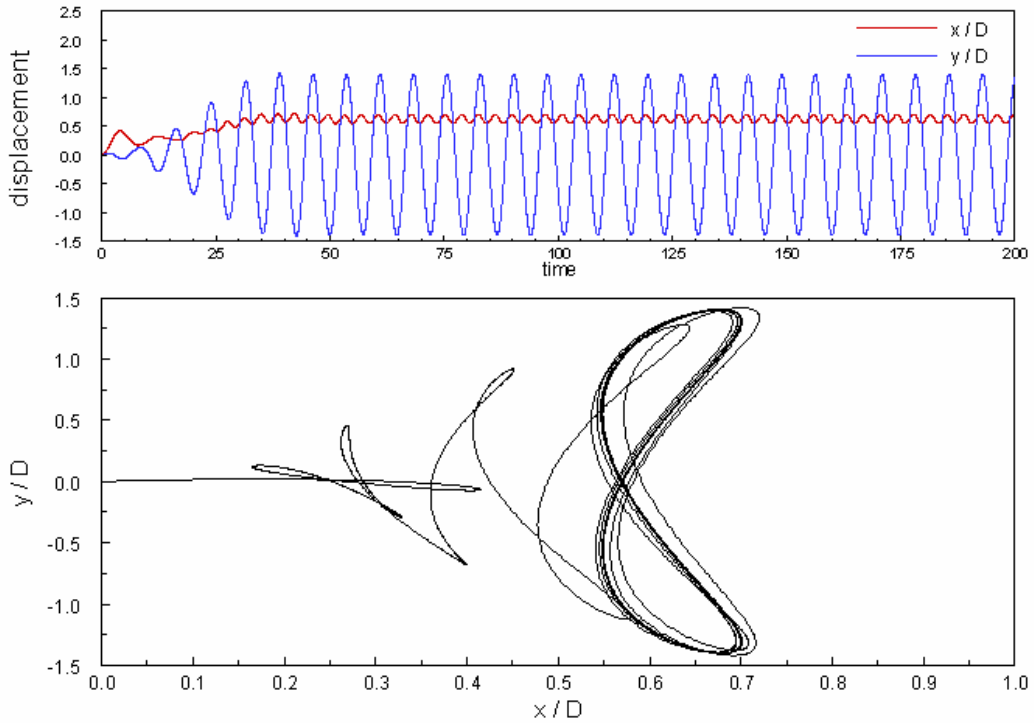


Figure 7: Circular cylinder undergoing VIV at $Re = 1 \times 10^6$. (a) Time history of cylinder's cross-stream and in-line displacements. (b) Trajectory of the cylinder in $x - y$ space for $t \in [0, 200]$.

2.5 Large Eddy Simulation of 3D Flow Past a Fixed Circular Cylinder

As noted earlier, the flow past a circular cylinder is three-dimensional when the Re is greater than 188.5. Furthermore, the wake behind the cylinder becomes turbulent for moderate Reynolds numbers, $O(10^4) - O(10^5)$ even though the boundary layer flow remains laminar. In order to provide adequate resolution of the three-dimensional transitional flow at moderate Reynolds numbers, large eddy simulations (LES) were also performed for flow past a short three-dimensional cylinder with a span-to-diameter ratio of 2:1. In the present large eddy simulations, the large scale vortices are resolved directly using the filtered Navier-Stokes equations and the sub-grid turbulence is modeled using the Smagorinsky model. The solution domain is divided into two blocks with a $182 \times 41 \times 34$ cylindrical grid embedded in a $201 \times 101 \times 34$ background rectangular grid. Simulations were performed at $Re = 1 \times 10^5$ for 18,000 steps with a time increment of 0.01.

Figure 8 shows the spanwise vorticity contours in the mid-plane at 10 selected time instants. It is seen that the spanwise vortices behind the cylinder grow gradually during the initial stage of development, but remain symmetric up to $t = 20$. However, there is a continuous growth in the spanwise velocity component and the flow becomes increasingly three-dimensional after $t = 20$. The shear layer instability eventually leads to the shedding of small scale eddies in the near wake region as seen in the snapshots between $t = 30$ and 36. The shedding of large scale eddies was observed after $t = 40$ and quickly reached full strength in a few shedding cycles. However, the drag and lift force histories display typical chaotic behavior since the flow is no longer periodic at this Reynolds number.

Figure 9 shows the iso-surface (i.e., constant vorticity) of the spanwise vorticity contours at $t = 180$. It is clearly seen that the flow is nearly two-dimensional immediately behind the cylinder, but becomes increasing three-dimensional further downstream. In order to obtain a more detailed understanding of the three-dimensional shear layer instability, the iso-surfaces of streamwise vorticities were superimposed on top of the spanwise vorticity contours as shown in Figure 10. It is noted that the streamwise vorticities are generated inside the cylinder boundary layer and shed downstream. These iso-surfaces of the streamwise vorticity clearly exhibit a three-dimensional coherent structure in the spanwise direction. The spanwise variation of the Karman vortex street at various cross-sections along the cylinder can also be clearly seen in Figure 11.

In order to evaluate the feasibility of large eddy simulation for riser VIV, calculations were also performed for a 2D circular cylinder undergoing 2-dof VIV motions using a two-dimensional LES code. In this case, the Smagorinsky model was modified by taking area-average instead of volume-average for the sub-grid eddy viscosity. Figure 12 shows the vorticity contours and velocity vectors at $t = 90$ and 200. Both the flow field and the predicted drag and lift force histories appear to be quite reasonable. However, we are still searching for available experimental data in order to provide a thorough validation of the 2-dof VIV simulation results for both the RANS and LES codes.

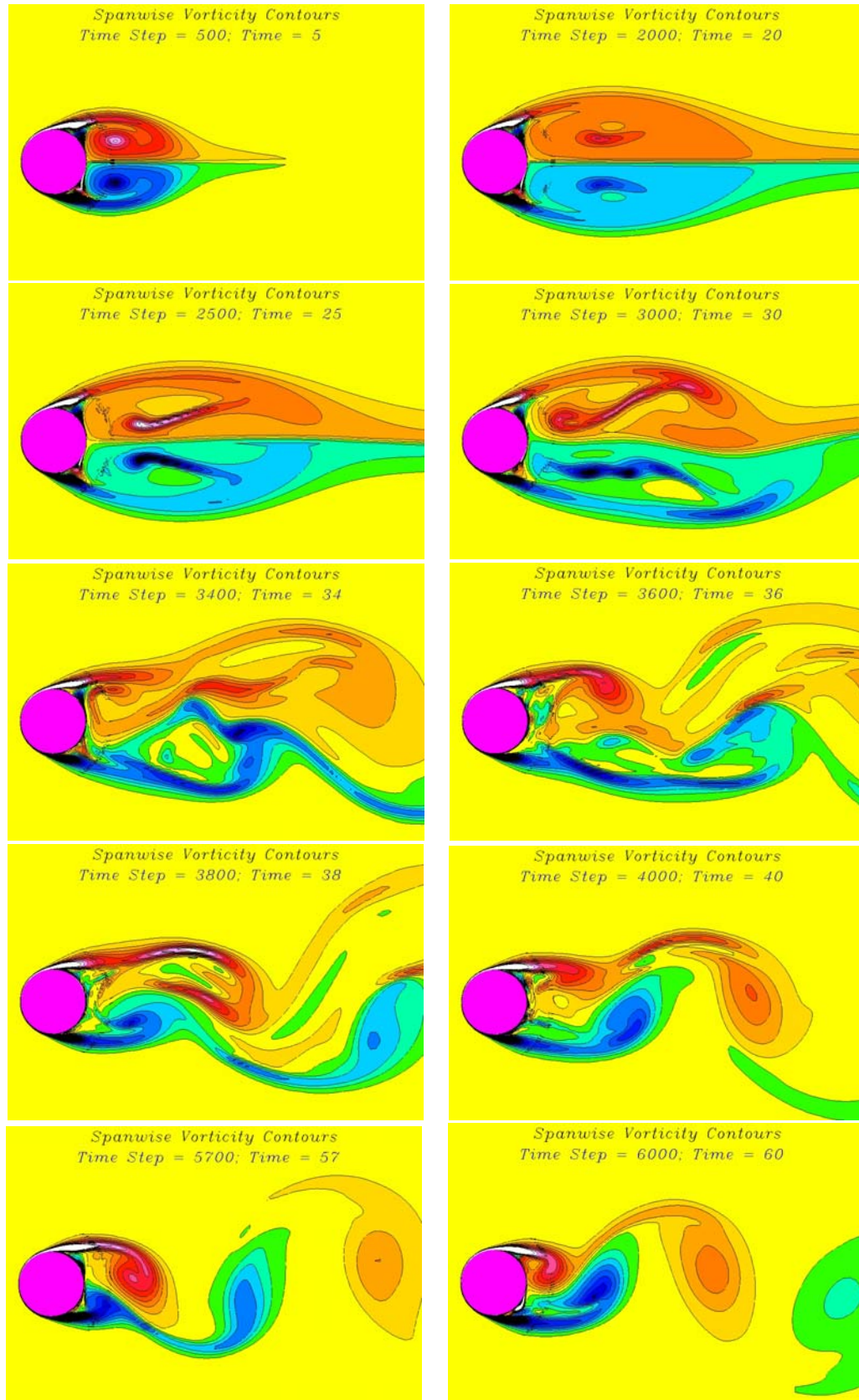


Figure 8: Spanwise vorticity contours in the mid-plane; large eddy simulation results at $t = 5, 20, 25, 30, 36, 38, 40, 57, \text{ and } 60$; $\text{Re} = 1 \times 10^5$.

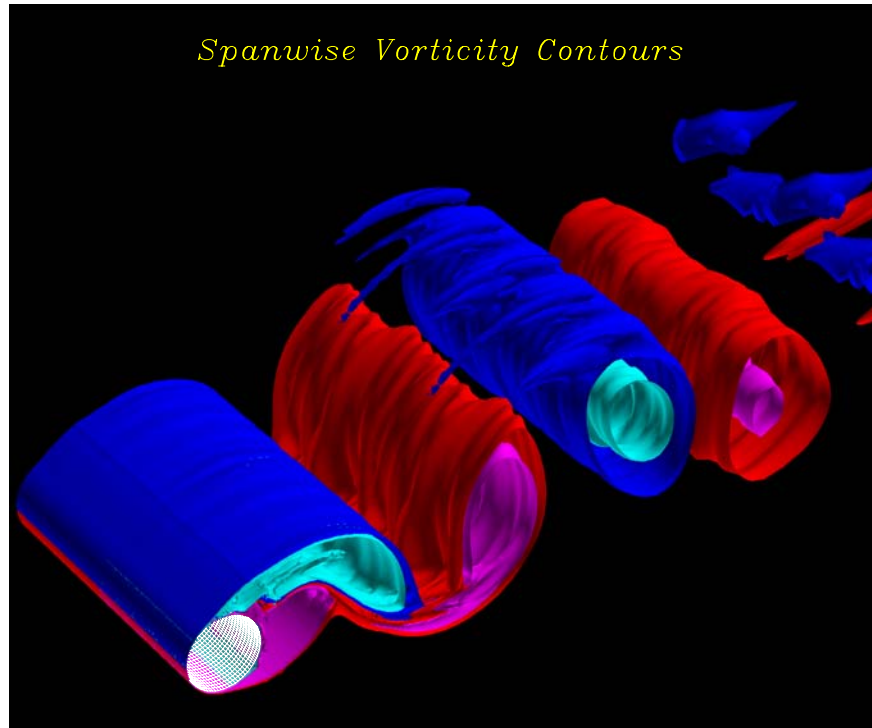


Figure 9: Spanwise vorticity contours; large eddy simulation; $Re = 1 \times 10^5$.

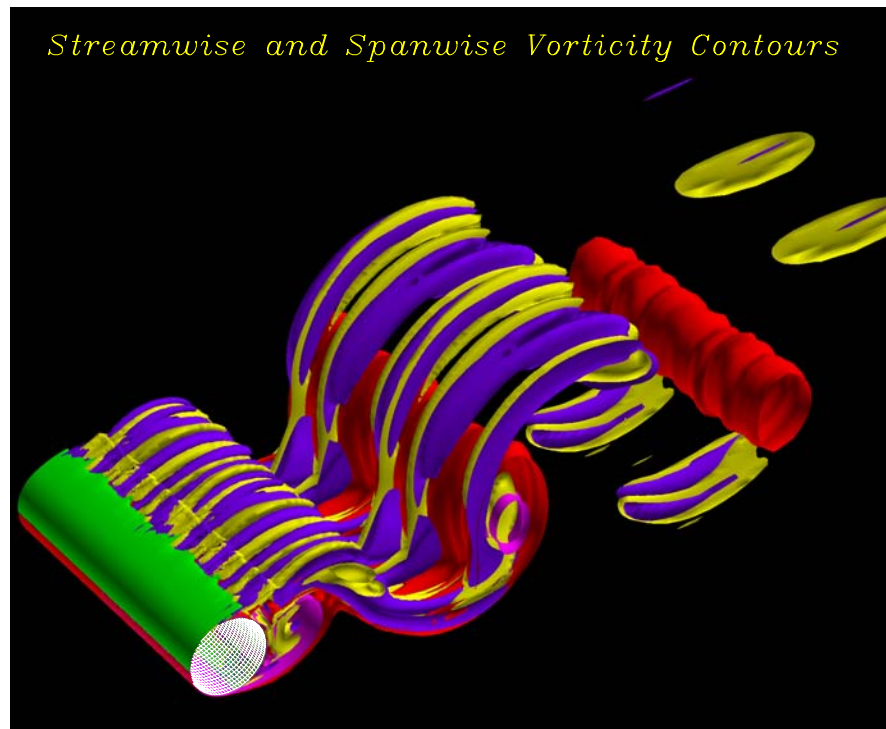


Figure 10: Streamwise and Spanwise vorticity contours; large eddy simulation; $Re = 1 \times 10^5$.

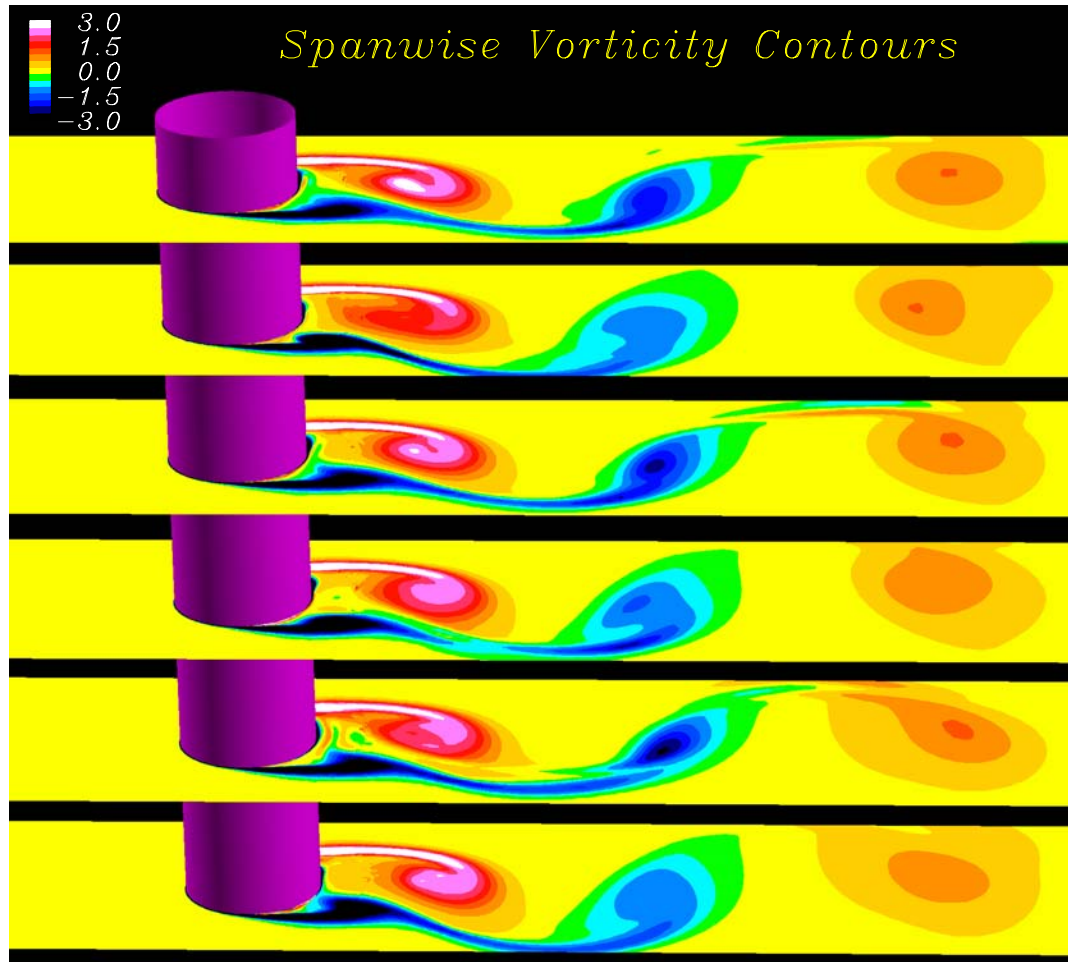


Figure 11: Spanwise vorticity contours at selected stations; large eddy simulation.

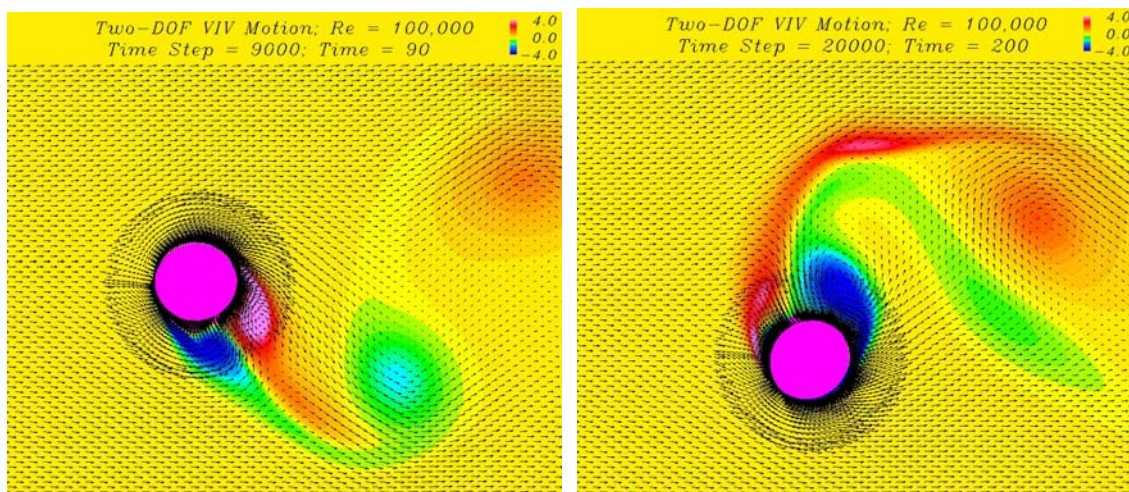


Figure 12: Two-dof VIV motion; large eddy simulation, $Re = 1 \times 10^5$.

3. Focus for 2004-2005 and anticipated results

The focus of the second year (2004-2005) project is concerned with the following tasks:

- Development of *new* surface roughness model
- Simulations of *arrays* of circular cylinders undergoing VIV
- Development of advanced CFD capabilities: multi-processor parallelization
- Simulations with VIV suppressors including fairings and strakes

With the new surface roughness model in place, we will be able to make direct comparisons with experimental data – as the bulk of experimental measurements for VIV are for rough cylinders. In preparation for the three-dimensional studies, we will start the parallelization of the CFD code – which will speed up computations linearly with the number of processors.

Simulations of multiple riser interactions around riser arrays will also be performed. We will investigate the wake interference effects for various two-dimensional riser array configurations, including tandem, side-by-side, and staggered arrangements. In addition, numerical simulations for single cylinders outfitted with VIV suppressors will be performed, either for two-dimensional flow or a short section of the three-dimensional riser under uniform current conditions.

Reports and Publications

- [1] Pontaza JP, Chen HC, Reddy JN. “A local-analytic-based discretization procedure for the numerical solution of incompressible flows.” *International Journal for Numerical Methods in Fluids*, 2004; submitted.
- [2] Pontaza JP, Chen CR, Chen HC. “Chimera Reynolds-averaged Navier-Stokes simulation of vortex-induced vibrations of circular cylinders.” *Conference Proceedings: Civil Engineering in the Oceans VI, 2004*; Baltimore, Maryland.